UCLA
UCLA Previously Published Works

Title

Methodology for computing white matter nerve fiber orientation in human histological slices.

Permalink

Authors

Nazaran, Amin
Wisco, Jonathan J
Hageman, Nathan
et al.

Publication Date

DOI

Peer reviewed

Methodology for computing white matter nerve fiber orientation in human histological slices

Amin Nazaran[a], **Jonathan J. Wisco**[b], **Nathan Hageman**[c], **Stephen P. Schettler**[c], **Anita Wong**[c], **Harry V. Vinters**[c], **Chia-Chi Teng**[d], and **Neal K. Bangerter**[a]

[a]Electrical and Computer Engineering Department, Brigham Young University, 437 CB Provo, Utah 84602

[b]Department of Physiology and Developmental Biology, and Neuroscience Center, Brigham Young University, Provo, UT 84602; Department of Neurobiology and Anatomy, University of Utah School of Medicine, Salt Lake City, UT 84132

[c]Department of Pathology & Laboratory Medicine, David Geffen School of Medicine at UCLA, Los Angeles, CA

[d]School of Technology, Brigham Young University, 265 CTB Provo, Utah 84602

Abstract

Background—The gold standard for mapping nerve fiber orientation in white matter of the human brain is histological analysis through biopsy. Such mappings are a crucial step in validating non-invasive techniques for assessing nerve fiber orientation in the human brain by using diffusion MRI. However, the manual extraction of nerve fiber directions of histological slices is tedious, time consuming, and prone to human error.

New Method—The presented semi-automated algorithm first creates a binary-segmented mask of the nerve fibers in the histological image, and then extracts an estimate of average directionality of nerve fibers through a Fourier-domain analysis of the masked image. It also generates an uncertainty level for its estimate of average directionality.

Results and Comparison with Existing Methods—The average orientations of the semi-automatic method were first compared to a qualitative expert opinion based on visual inspection of nerve fibers. A weighted RMS difference between the expert estimate and the algorithmically-determined angle (weighted by expert's confidence in his estimate) was 15.4 degrees, dropping to 9.9 degrees when only cases with an expert confidence level of greater than 50% were included. The algorithmically-determined angles were then compared with angles extracted using a manual segmentation technique, yielding an RMS difference of 11.2 degrees.

Conclusion—The presented semi-automated method is in good agreement with both qualitative and quantitative manual expert-based approaches for estimating directionality of nerve fibers in white matter from images of stained histological slices of the human brain.

Keywords

Histology; White matter; Nerve fibers; orientation map; Fiber tracking; Nerve fibers Orientation; Fourier Transform; Average orientation

1. Introduction

Diffusion Magnetic Resonance Imaging (dMRI) is an imaging technique that measures the properties of water diffusion in tissues, and has revolutionized the study of brain anatomy. Prior to the development of dMRI, traditional approaches to study white matter could only be done post-mortem. The impact of diffusion MRI techniques on the study of neurological disease has been widespread.

Diffusion MRI techniques can produce estimates of water diffusivity in multiple directions, allowing the estimation of a "diffusion tensor" for each imaged voxel that is directly related to the potentially anisotropic restriction of water diffusion [1, 2, 3]. This is termed Diffusion Tensor Imaging, or DTI. The restriction of water diffusion is influenced by underlying microstructural anatomy. In white matter, fiber bundles contribute the most to anisotropic diffusion [2, 4]. The linearity of successively adjacent diffusion tensors is calculated to reconstruct fiber bundles. Disease-related changes in the fiber bundles can thus be identified, as (for example) demonstrated in recent studies of Alzheimer's disease [5, 6, 7, 8, 9, 10, 11]. Further studies have shown a direct relationship between white matter fiber structure and AD cognitive impairment [5, 9, 11, 12].

Validation of DTI is crucial for assessing its reliability and accuracy of measuring white matter diffusion. The algorithms that approximate the underlying white matter architecture need to be accurate. For obvious reasons, a true anatomical comparison for DTI validation is not feasible clinically in humans, but has been attempted in phantom [13, 14] and animal studies [15, 16]. Examples include tractography validation with excised rat spinal cords [17] and enhancement of the optic tracts by the injection of manganese ions [14].

In studies of human white matter structure and fiber reconstruction, references to anatomical correlates have been qualitative, referring only to already established histological anatomy (e.g., [18]). In AD, white matter degeneration measured with DTI is associated with the progression of cognitive impairment [5, 9, 11, 12]. However, validation of white matter segmentation in DTI has been mostly limited to qualitative comparisons of results to known anatomical connectivity by a skilled neuroanatomist. There is no resource that exists to permit a direct comparison of DTI data to the underlying white matter architecture.

The creation of a methodology for the direct comparison of DTI data with actual underlying white matter architecture is an extraordinarily difficult problem. This paper focuses on one aspect of this problem: namely, the detection of two-dimensional vectors representing white matter fiber orientations in stained histological sections of the post-mortem human brain.

Tissue sections stained specifically for white matter fibers provide qualitative directionality of tracts, but the systematic measurement of the orientation of fibers in histological slices such that they can eventually be directly compared to DTI data is challenging. Examples of published techniques seeking to validate diffusion MRI with histology include those using 2D structure tensors [19, 20, 21], Fourier analysis [22], wavelet decomposition [23], oriented filtering [24], micrographs [25], and template matching [26]. While the resolutions achievable with DTI are much lower than those in images of histological sections, and DTI inherently provides three-dimensional information, the extraction of two-dimensional directionality of white matter tracts from images of histological slices is nevertheless an important step in a direct comparison of DTI data to the underlying white matter architecture.

This is particularly important as DTI techniques improve and are extended, and the ability to infer white matter structure on a finer scale increases. Identifying fiber directionality in histological slices has typically involved manual assessment of fiber direction by a trained observer, and is tedious, slow, highly labor intensive, and fatiguing. Furthermore, reproducibility may be poor [27, 28].

In this paper, we present an algorithm for the semi-automated assessment of fiber directionality from high-resolution images of stained histological sections of the post-mortem human brains. Images of histological sections are divided into subsections which we term "panels". The algorithm then extracts both an average two-dimensional directionality for each panel and an estimated uncertainty level for the directionality vector. The algorithm is rapid and computationally efficient, and is based on a Fourier-domain analysis of a color-thresholded image of each panel.

We assessed the performance of the algorithm by having a trained neuroanatomist assess the directionality in six histological slices (each from a different post-mortem brain) divided into a total of 300 sub-regions of varying dimensions. The weighted [1] RMS difference between the algorithmically-determined values and the expert-determined values was then calculated to give an indication of algorithmic performance. We further compared the performance of the algorithm to the angles extracted using a time and labor intensive manual segmentation technique. In both cases, the RMS difference was below 16 degrees, and dropped to below 10 degrees in the qualitative comparison against the expert opinion when only panels where the expert ascribed 50% or greater confidence to his estimate were included in the analysis.

2. Materials and Methods

Tissue preparation and imaging: Formalin fixed hippocampal specimens were blocked in the coronal plane with a thickness of 2.5mm and embedded in paraffin. The tissue was obtained from the Neuropathology Core at the David Geffen School of Medicine at UCLA. Sections were cut in 10 micron sections using a Leica rotary microtome and then stained with Luxol Fast Blue/cresyl violet, which stains white matter fibers dark blue and nuclei deep purple. After preparation and staining, each histological slice was scanned using a

---

[1]weighted by the confidence of the neuroanatomist on his determination of the directionality

Leica SCN400 slide scanner at 20× magnification and panels were visualized using the Leica Virtual Microscopy (Leica Biosystems Inc., Germany).

Terminology: In this manuscript, we will refer to a high resolution image of a stained slice as a "histological slice". Histological slices are then subdivided into regions of interest, "ROIs", that we wish to analyze in more detail. Finally, each ROI is subdivided into "panels", each of which is analyzed for average directionality of white matter tracts across the panel. In other words, our algorithm will operate at the panel level, identifying a single 2D vector representing average directionality for that panel, along with a single estimate for the uncertainty of the direction for that panel.

2.1. Algorithm

A representative panel from a ROI in the white matter of a histological slice is shown in Figure 1. Nerve fibers tend to be dark blue or purple on these stained histological images. Our algorithm attempts to (1) isolate or segment the nerve fibers in the panel, (2) construct an angular histogram that represents the dominance of nerve fiber orientation in each direction, and (3) extract an "average" directionality from the angular histogram, along with an estimate for the uncertainty in the directionality.

2.1.1. Segmentation of nerve fibers in a panel—Segmentation of the nerve fibers in a panel can be accomplished by a threshold based algorithm applied after the panel image is mapped to an appropriate color space. Human vision is perceptually uniform, meaning that we can distinguish the nerve fibers from other structures because variations in color across nerve fibers are relatively small compared to the color differences between completely different structures. From an algorithmic point of view, we can automate this process more accurately by choosing a color space for the images which minimizes color variations across nerve fibers while preserving a stark difference in color between nerve fibers and other structures [29, 30]. The RGB color space (the default for our histological slices) is not well suited for the proposed segmentation algorithm. However, the LAB color space is perceptually uniform [31, 32, 33, 34, 35], and a better choice for our algorithm.

The LAB color space consists of 3 channels: a luminosity channel and two color channels. We found that segmentation was most robustly done on the luminosity channel image, although sometimes information from the two color channels can improve segmentation on the luminosity channel. Our segmentation algorithm consists of the following four steps, which are summarized in Figure 2:

1.   Convert all histological panels from RGB to LAB.

2.   Apply a threshold on the luminosity channel of the first panel using maximum and minimum thresholding values manually determined by the user to separate nerve fibers from surrounding structures.

3.   If this simple luminosity-channel thresholding fails to effectively segment nerve fibers, then a threshold is applied on one of the color channels to identify non-nerve fiber structures. This can then be subtracted from the luminosity-channel thresholded image to improve segmentation of nerve fibers.

4. Once the above steps are completed, we are left with a binary image that contains both actual nerve fibers and some undesired structures (i.e., blood vessels and glia). Fortunately, true nerve fibers tend to occupy a much larger contiguous area than the undesired structures introduced in this process. In this final segmentation step, the areas of contiguous structures in the binary image are computed, and those below a minimum threshold (which are unlikely to be nerve fibers) are deleted.

The segmentation step is now done, yielding a binary mask indicating where nerve fibers are in the panel. Figure 3 illustrates the steps described above to make a binary mask of nerve fibers from a representative panel.

2.1.2. Construction of orientation-based angular histogram—Once the segmentation step is done, we analyze the angular distribution of all of the nerve fibers identified in a given panel. However, the identification of a single "direction" for each identified nerve fiber is not easily done. Our algorithm employs a Fourier-domain technique for estimating the dominance of different directions in the segmented image, allowing the construction of an orientation-based angular histogram for each panel. This histogram can then be analyzed to identify the average directionality in the panel. The spread of the angular distributions across the panel can be used to derive an estimate of the uncertainty for the average directionality in the panel.

The presence of sharp edges in a given direction in an image manifests as increased energy in the high spatial frequencies of the Fourier representation of the image. This increase is in angular regions perpendicular to the direction of sharp edges in the image domain. This is illustrated in Figure 4(a-d). Thus, by analyzing the angular distribution of energy in the high spatial frequencies in the Fourier domain, we can identify directions present in the segmented image of a panel, and estimate how strongly each of those directions is represented.

To produce an angular histogram for a given panel, the following steps are performed:

1. Take the 2D Discrete Fourier Transform (DFT) of the panel.

2. Mask out the low spatial frequencies in the DFT image of the panel (equivalent to applying a high-pass filter to the original panel image).

3. Divide the remaining portion of the image into "angular windows" as illustrated in Figure 5. Once divided, we sum the energy in each window, and use these sums to form an orientation-based histogram where the intensity of the histogram at a given angle is equal to the image energy found within the corresponding angular window.

Variable parameters for this process include the cut-off spatial frequency of the high-pass filtering step r_c (measured in pixels in the Fourier domain image), the angular window width a, and the angular spacing ψ between sliding-angular-window bins (Figure 5). Note that a maps to the angular extent of each bin in the angular histogram. We use Ψ to denote the

angle of a radial line passing through the center of an angular window. The algorithm thus analyzes angular windows with Ψ ranging from 0 to 179 degrees in increments of Ψ.

Let $F(k_x, k_y) = \mathcal{F}\{f(x, y)\}$ represent the 2DFT of the thresholded panel image, where k_x and k_y are spatial frequencies in the x and y directions respectively. The energy, ε, in an angular slice of angular width a centered at angle Ψ is then given by:

$$\varepsilon(\psi) = \sum_{w=\psi-\alpha/2}^{\psi+\alpha/2} \sum_{r=r_c}^{\text{floor}[M/|(2\cos(w))|]} |\mathbf{F}[r\cos(w), r\sin(w)]|^2 \qquad (1)$$

where M and N are the width and height of the image (in pixels), and r_c is the cut off radius (also in pixels).

Again, it is important to note that the orientation of the nerve fiber edges in the masked image are perpendicular to the observed orientation of the edges in the Fourier domain. The dominant direction of each of the panels is apparent as a line of increased energy in the Fourier domain at an angle perpendicular to the dominant direction in the panel. This line in the Fourier domain results from the sharp edges that are present in the mask image.

Note that the angular window size a, cut-off frequency r_c, and angular increment Ψ should be carefully chosen to yield the best results for a given application. For example, increasing window size reduces angular resolution and smooths the energy histogram distribution. Increasing the cut-off frequency r_c changes the strength of the dominant directions. Changing angular spacing alters the histogram resolution. Note that the angular histogram can be visualized either as a standard cartesian histogram or as a polar histogram.

2.1.3. Orientation estimation from orientation-based angular histogram—Once an orientation-based histogram is generated for each panel, we can extract a simple average orientation and an estimate of the uncertainty for that panel. While it is tempting to simply find a weighted mean of the histogram (similar to finding the statistical mean of a probability mass function), this can produce undesired results if a peak is centered near 0 and/or 180 degrees as in (Figure 6(b)). This problem can be avoided by extending the angular histogram to cover a range of 0 to 359 degrees (effectively replicating it twice). We then calculate the mean and standard deviation of a sliding window with a 180 degree width, starting with a window from 0 to 179 degrees and finishing with a window from 180 to 359 degrees. We then choose the window that has the lowest standard deviation, as illustrated in Figure 6(c). In most cases, this will concentrate a directional peak towards the center of the angular window, and yield more accurate results when a peak is clustered near the edges of the 0 to 179 degree window.

Once the sliding window that yields the minimum standard deviation is identified, the average orientation for the panel is then simply computed as the weighted mean of the angular histogram over that minimum standard deviation window. We use the standard deviation of the angular histogram over the minimum standard deviation window as our measure of the uncertainty, where a smaller standard deviation indicates a higher level of

confidence in our angular estimate. After extracting the average orientation from the angular histogram for a panel, other useful information can be extracted from the histogram based on the degree to which it is uni-modal vs. multi-modal.

2.2. Manually marking fibers

For comparison, we manually marked fiber directions in 50 panels using the following 3-step process. First, vector lines were drawn close to the nerve fibers using the Neurolucida (Microbrightfield Bioscience, Vermont) such that the length and the direction of the lines represented the respective dimensions of the nerve fibers. We used the operational definition of nerve fibers as being visually discernible from a clear beginning and end within the plane of the tissue section. An angular orientation histogram from 0 to 179 degrees was then created, with bins centered at each degree. The height of each bin was the total sum of the lengths of the lines within the angular range of each bin. We then followed the same procedure as described in section 2.1.3 to estimate the average orientation and find the standard deviation.

3. Experimental setup

The algorithm described above were implemented in MATLAB (The Math-Works, Inc., Massachusetts). We describe other aspects of our experimental set up below.

3.1. Selection of algorithmic parameters

Selection of threshold—Minimum thresholds were manually chosen for six stained batches. Staining variations from batch to batch can be significant, so this step is important for tuning algorithmic performance. Minimum thresholds were chosen such that the thresholded images contain a minimum amount of undesired structures (i.e., blood vessels and glia). The binary masked images of the undesired structures and the nerve fibers were compared visually, one by one, to the original non-masked images of the panels. The thresholding values that matched the location and width of the undesired structures and the nerve fibers in the panel (by visual inspection) were chosen.

Selection of a, r_c, and Ψ—In our experiments, other algorithmic parameters were determined by evaluating eight panels with one dominant nerve fiber orientation and sixteen panels with at least two dominant nerve fiber orientation across a range of parameter values. The resulting angular orientation histograms of each of the 24 panels were then visually inspected, and a determination made on which sets of parameters best yielded angular histograms with dominant peaks around the expert's assessment of fiber orientation in the corresponding panels. Parameter values were varied as follows: r_c was varied from 2 to 25 pixels (in 1 pixel increments) while fixing $a = 1$ degree and $\Psi = 1$ degree. A visual inspection was then performed to determine a good value of the cut-off frequency r_c. This value of r_c was then used going forward, and the value of a was varied from 1 to 6 degrees (in 1 degree increments) while keeping $\Psi = 1$. A visual inspection was then performed to determine the best value of a. Finally, the process was repeated with r_c and a fixed at the previously-determined values, and Ψ was varied. For the histological panels examined, the

following values were found to yield reasonable results, and were then used in all subsequent experiments: $a = 2$ degrees, $r_c = 15$ pixels, and $\Psi = 1$ degree.

3.2. Qualitative validation of the semi-automated method

A qualitative evaluation of the semi-automated method was performed by an expert neuroanatomist (J.J.W.) in the following manner. Panels were drawn from ROIs in six histological slices (from six different subjects, 1 histological slice per subject). The performance of the algorithm was tested across 134 randomly-selected panels of different physical dimensions (692mm × 692mm and 776mm × 776mm) all rendered to 512×512 pixels to ascertain how the algorithm performed across two different physical panel dimensions (These 134 panels were selected from data sets 6 and 7 of Table I.) The neuroanatomist was first shown all 134 panels, and asked to visually inspect each panel and assign a dominant nerve fiber direction to each panel. In addition, he was asked to assign a confidence level from 0 (least confident) to 1 (most confident) in his estimate of directionality for each panel. These expert-determined directionalities were then subtracted from the corresponding algorithmically-determined values, and a weighted root-mean-square (RMS) value determined across the 134 panels. The weightings used were the expert-assigned confidence estimates.

A second qualitative experiment was performed in which the neuroanatomist was shown the algorithmically-determined directions and uncertainty levels for each of a sample of 300 panels drawn from these panels summarized in Table 1. He was then asked to make a binary determination, yes or no, on whether the algorithmically-determined directionality and confidence estimate was reasonable based on his expert visual inspection of the corresponding panel. He was also shown the algorithmically-generated angular histograms for each panel, and asked to make a binary determination on whether the dominant nerve fiber direction (if any) visually evident to him on the polar histogram was reasonably captured in the algorithmically-determined angular estimate.

3.3. Quantitative comparison of the semi-automated method to manual segmentation

A quantitative comparison of our semi-automated method to a manual-segmentation-based method was then performed using a single histological slice from a single subject (dataset 6 in Table 1). Two trained graduate anatomy students manually marked [2] fibers for a ROI in the histological slice. Then, the ROI was divided into 50 panels, each with a size of 512×512 pixels matrix and physical panel size of 500mm×500mm. An angular histogram was then produced based on the manual marking containing 180 bins over the range of 0 to 179 degrees. The values in each bin corresponded to how many lines in the panel were marked in that angular direction, weighted by the length of the marked lines (corresponding to the visually-determined length of the nerve fiber) as previously described. Once these angular histograms were produced from the manually-marked panels, the average directionality and uncertainty level was extracted from these histograms using the same algorithm (described above) used in the semi-automated technique.

---

[2] Manually segmenting fibers using operational definition of dark blue stained curvilinear structures with a distinguishable beginning and end.

The semi-automated algorithm was then performed on each of the 50 panels, and average directionality and uncertainty levels extracted. The parameters in sub-section 3.1 were used for the semi-automated algorithm. The two angular estimates for each panel (those from the manual marking and those from the semi-automated algorithm) were then subtracted, and a root-mean-square (RMS) value determined across all 50 panels.

4. Results

4.1. Qualitative validation of the semi-automated method

The weighted RMS difference between the expert neuroanatomist directionality determinations and the semi-automatic algorithm for the 134 panels studied was 15.4 degrees. However, when only panels were taken into consideration with an expert-determined confidence level of 50 percent or more, the weighted RMS difference dropped to 9.9 degrees.

The qualitative binary determination of the expert neuroanatomist across the 300 panels revealed that the expert was in all cases comfortable with the directionality estimates of the algorithm, and that the algorithmically-produced angular histograms revealed the structure he expected to see based on visual inspection of the panel in all cases. While we recognize the limitations of this kind of comparison, the results did give us confidence in the ability of the algorithm to produce what would be deemed reasonable estimates based on expert evaluation of the panel under consideration.

Finally, for illustration of algorithmic performance, a region of interest containing 123 panels is shown in Figure 7, with average orientation shown as a line for each panel. The length of the line indicates the uncertainty of the confidence in the angular estimate (with longer lines indicating a lower level of uncertainty). In addition, the polar histograms and the average orientation for four panels are illustrated.

4.2. Quantitative comparison of the semi-automated method to manual segmentation

The RMS difference in average directionality was calculated across the 50 panels manually segmented and found to be 11.2 degrees.

5. Discussion

We are encouraged by the performance of the semi-automated approach in the various comparisons conducted, and believe that it could be a valuable additional tool in the ongoing effort to validate the accuracy of DTI techniques using histology. The results of the algorithm are in reasonable agreement with those obtained through visual inspection by the expert anatomist, and are in even better agreement when compared only to panels in which the expert expressed a high degree of confidence in his estimate. Furthermore, the results were in good agreement with the much more labor and time intensive manual segmentation technique. However, it is important to note that validation of an algorithm such as this is inherently limited by the lack of a gold standard with which to compare. The comparison studies shown are a first step in this process, and future work is needed to more fully validate the algorithm against the wide variety of other techniques that can be applied to the same

problem. It is beyond the scope of this paper (intended to introduce the algorithm and provide a basic demonstration of its utility) to provide a more exhaustive comparison against the broad range of other competing techniques.

We were further encouraged by the purely qualitative and binary assessment performed by our expert anatomist. The trained human eye is very good at identifying approximate fiber directions, and identifying dominant direction(s) from angular histograms. While not a conclusive or quantitative measure of performance, the assessment of a trained expert anatomist that the algorithm was in all trial cases producing a direction that was reasonable based on his visual perception is encouraging.

We made the further observation during the outlined studies that a low uncertainty level was produced by the algorithm in panels that clearly had a dominant orientation evident through visual inspection. For panels that exhibit more than one dominant nerve fiber orientation (again through visual inspection), the angular histogram exhibited the expected multiple peaks, and the algorithm yielded a higher level of uncertainty in the direction estimate. The qualitative opinion of the expert neuroanatomist was that visual inspection of the angular histograms in conjunction with the corresponding panel revealed not only the dominant nerve fiber direction(s) of the panel, but also less dominant directions that were not immediately obvious from inspection of the panel itself. While the comparisons indicate reasonably good agreement between expert opinion, manual segmentation, and the proposed semi-automated algorithm, the differences observed could arise from the ability of the semi-automated algorithm to measure subtle directional trends not obviously visible to the human eye.

The differences between the manual segmentation and semi-automated techniques may also be due to the very different ways in which the two algorithms go about creating the angular histograms. Nevertheless, for panels that exhibit a single strong dominant direction, the polar histograms extracted from the manual segmentation technique were visually very similar to those extracted from the semi-automated algorithm. In some cases, however, both algorithms yielded very different looking polar histogram shapes, but a very similar dominant direction. In these cases, the manual segmentation technique is likely simply not marking relatively small or non-dominant nerve structures that appear in the semi-automated technique. In cases where the directionality estimate from the manual segmentation diverged significantly from the estimate using the semi-automated algorithm, a post hoc informal inspection by the expert anatomist of both analyses was performed. In these cases, the anatomist concluded that the estimate of the semi-automated algorithm was more accurate in a significant majority of cases. Irrespective of these slight variations in performance, the presented Fourier-domain technique appears to be a viable substitute for manual segmentation techniques or expert assessment, and has the potential to be very rapid as the only manual step is tuning the thresholding values for each batch of histological slices.

The proposed technique has some clear limitations. As the variability of the nerve fiber orientations increases, the standard deviation for the panel also increases and the average orientation measurement is less likely to be a good representation of the different orientations existing in a panel. An additional limitation of the technique is sensitivity to

lighting and variations in staining. A more thorough study of the effects of these variations on algorithmic performance is needed, but was not possible with our limited dataset and is beyond the scope of this paper. Finally, another clear limitation of the algorithm is its inability to accurately assess through-plane fiber directionality, given the 2D nature of the images of these thin histological slices. It also should be noted that better techniques may exist for locating the dominant direction of the angular histogram (such as through peak detection algorithms), and the technique could be extended in the future to attempt to identify multiple dominant directions in the angular histograms.

Future work should focus on (1) further validation of the algorithm through more thorough comparisons with other techniques, (2) assessment of the sensitivity of the algorithm to lighting and variations in staining (i.e., Luxol Fast Blue/cresyl violet versus Luxol Fast Blue/ hematoxylin and eosin), and (3) evaluation of potential improvements in the interpretation of the produced angular histograms.

Once the algorithm has been more thoroughly validated and tuned, we hope to use it to correlate the average directionality of nerve fibers in histological slices with the directionality of fiber bundles revealed using diffusion tensor MRI on the brain prior to histological evaluation. As previously mentioned, this is a challenging problem for a variety of reasons. Voxel sizes in DTI datasets will typically be 1-2mm isotropic; the histological slices are much thinner, and the resolution of histological images after staining is much higher in-plane. Furthermore, the DTI datasets reveal fiber orientation in three dimensions (including the through-plane direction), while the data extracted from the histological slices fails to capture through-plane fiber orientations. Finally, registration of thin, high-resolution histological images to the corresponding much lower resolution DTI data will be challenging due to differences in resolution and orientation, and sample warping during histological preparation. Nevertheless, it should be possible to validate clear in-plane fiber orientations observed in the DTI datasets with the corresponding histological images, and extract some information about through-plane directionality from series of 2D histological slices.

6. Conclusion

In this paper, we have presented a robust and semi-automated technique for extracting nerve fiber orientation from images of stained histological slices, along with an estimate of uncertainty in the extracted direction. Qualitative evaluation of the new technique by an expert neuroanatomist indicates that the semi-automated technique is indeed accurately identifying what the neuroanatomist would consider the dominant nerve fiber orientation based on visual inspection. Furthermore, the algorithm appears to take into consideration nerve fiber microstructure that is not immediately evident from rapid visual inspection. Quantitative comparison of the new semi-automated algorithm against a more time and labor intensive manual nerve fiber segmentation technique suggests that both techniques yield similar results, further bolstering confidence in the accuracy of the semi-automated approach.

Acknowledgments

References

1. Basser PJ, Pierpaoli C. Microstructural and physiological features of tissues elucidated by quantitative-diffusion-tensor {MRI}. Journal of Magnetic Resonance. 2011; 213(2):560–570. doi: http://dx.doi.org/10.1016/j.jmr.2011.09.022. URL http://www.sciencedirect.com/science/article/pii/S109078071100334X. [PubMed: 22152371]

2. Beaulieu C. The basis of anisotropic water diffusion in the nervous system a technical review. NMR in Biomedicine. 2002; 15(7-8):435–455. URL http://dx.doi.org/10.1002/nbm.782. DOI: 10.1002/nbm.782 [PubMed: 12489094]

3. Basser PJ, Jones DK. Diffusion-tensor mri: theory, experimental design and data analysis a technical review. NMR in Biomedicine. 2002; 15(7-8):456–467. URL http://dx.doi.org/10.1002/nbm.783. DOI: 10.1002/nbm.783 [PubMed: 12489095]

4. Beaulieu C, Allen PS. Determinants of anisotropic water diffusion in nerves. Magnetic Resonance in Medicine. 1994; 31(4):394–400. URL http://dx.doi.org/10.1002/mrm.1910310408. DOI: 10.1002/mrm.1910310408 [PubMed: 8208115]

5. Wang L, Goldstein F, Veledar E, Levey A, Lah J, Meltzer C, Holder C, Mao H. Alterations in cortical thickness and white matter integrity in mild cognitive impairment measured by whole-brain cortical thickness mapping and diffusion tensor imaging. American Journal of Neuroradiology. 2009; 30(5):893–899. arXiv:http://www.ajnr.org/content/30/5/893.full.pdf+html. URL http://www.ajnr.org/content/30/5/893.abstract. DOI: 10.3174/ajnr.A1484 [PubMed: 19279272]

6. Stricker N, Schweinsburg B, Delano-Wood L, Wierenga C, Bangen K, Haaland K, Frank L, Salmon D, Bondi M. Decreased whitematter integrity in late-myelinating fiber pathways in alzheimer'sdisease supports retrogenesis. NeuroImage. 2009; 45(1):10–16. doi: http://dx.doi.org/10.1016/j.neuroimage.2008.11.027. URL http://www.sciencedirect.com/science/article/pii/S1053811908012317. [PubMed: 19100839]

7. Medina DA, Gaviria M. Diffusion tensor imaging investigations in Alzheimer's disease: the resurgence of white matter compromise in the cortical dysfunction of the aging brain. Neuropsychiatric disease and treatment. 2008; 4(4):737–742. [PubMed: 19043518]

8. Choi SJ, Lim KO, Monteiro I, Reisberg B. Diffusion tensor imaging of frontal white matter microstructure in early alzheimers disease: A preliminary study. Journal of Geriatric Psychiatry and Neurology. 2005; 18(1):12–19. DOI: 10.1177/0891988704271763 [PubMed: 15681623]

9. Medina D, DeToledo-Morrell L, Urresta F, Gabrieli JDE, Moseley M, Fleischman D, Bennett DA, Leurgans S, Turner DA, Stebbins GT. White matter changes in mild cognitive impairment and AD: A diffusion tensor imaging study. Neurobiology of Aging. 2006; 27(5):663–672. [PubMed: 16005548]

10. Kavcic V, Ni H, Zhu T, Zhong J, Duffy CJ. White matter integrity linked to functional impairments in aging and early Alzheimer's disease. Alzheimer's and Dementia. 2008; 4(6):381–389.

11. Teipel SJ, Meindl T, Wagner M, Kohl T, Bürger K, Reiser MF, Herpertz S, Möller HJ, Hampel H. White matter microstructure in relation to education in aging and Alzheimer's disease. Tech Rep. 2009; 3doi: 10.3233/JAD-2009-1077

12. Bai F, Zhang Z, Watson DR, Yu H, Shi Y, Yuan Y. Abnormal white matter independent of hippocampal atrophy in amnestic type mild cognitive impairment. Neuroscience Letters. 2009; 462(2):147–151. doi: http://dx.doi.org/10.1016/j.neulet.2009.07.009. URL http://www.sciencedirect.com/science/article/pii/S0304394009009173. [PubMed: 19596405]

13. Leemans A, Sijbers J, Verhoye M, Van der Linden A, Van Dyck D. Mathematical framework for simulating diffusion tensor mr neural fiber bundles. Magnetic Resonance in Medicine. 2005; 53(4):944–953. URL http://dx.doi.org/10.1002/mrm.20418. DOI: 10.1002/mrm.20418 [PubMed: 15799061]

14. Lin CP, Wedeen VJ, Chen JH, Yao C, Tseng WYI. Validation of diffusion spectrum magnetic resonance imaging with manganese-enhanced rat optic tracts and ex vivo phantoms. NeuroImage. 2003; 19(3):482–495. doi: http://dx.doi.org/10.1016/S1053-8119(03)00154-X. URL http://www.sciencedirect.com/science/article/pii/S105381190300154X. [PubMed: 12880782]

15. DArceuil HE, Westmoreland S, de Crespigny AJ. An approach to high resolution diffusion tensor imaging in fixed primate brain. NeuroImage. 2007; 35(2):553–565. doi: http://dx.doi.org/10.1016/j.neuroimage.2006.12.028. URL http://www.sciencedirect.com/science/article/pii/S1053811906012390. [PubMed: 17292630]

16. Mori S, Itoh R, Zhang J, Kaufmann WE, van Zijl PC, Solaiyappan M, Yarowsky P. Diffusion tensor imaging of the developing mouse brain. Magnetic Resonance in Medicine. 2001; 46(1):18–23. URL http://dx.doi.org/10.1002/mrm.1155. DOI: 10.1002/mrm.1155 [PubMed: 11443706]

17. Campbell JS, Siddiqi K, Rymar VV, Sadikot AF, Pike GB. Flow-based fiber tracking with diffusion tensor and q-ball data: Validation and comparison to principal diffusion direction techniques. NeuroImage. 2005; 27(4):725–736. doi: http://dx.doi.org/10.1016/j.neuroimage.2005.05.014. URL http://www.sciencedirect.com/science/article/pii/S1053811905003411. [PubMed: 16111897]

18. Behrens TEJ, Johansen-Berg H, Woolrich MW, Smith SM, Wheeler-Kingshott CAM, Boulby PA, Barker GJ, Sillery EL, Sheehan K, Ciccarelli O, Thompson AJ, Brady JM, Matthews PM. Non-invasive mapping of connections between human thalamus and cortex using diffusion imaging. Nature neuroscience. 2003; 6(7):750–757. [PubMed: 12808459]

19. Seehaus A, Roebroeck A, Bastiani M, Fonseca L, Bratzke H, Lori N, Vilanova A, Goebel R, Galuske R. Histological validation of high-resolution dti in human post mortem tissue. Frontiers in Neuroanatomy. 2015; 9:1–12. DOI: 10.3389/fnana.2015.00098 [PubMed: 25657619]

20. Budde MD, Annese J. Quantification of anisotropy and fiber orientation in human brain histological sections. Frontiers in integrative neuroscience. 2013; 7(February):3. URL http://www.pubmedcentral.nih.gov/articlerender.fcgi?artid=3561729&tool=pmcentrez&rendertype=abstract. doi: 10.3389/fnint.2013.00003 [PubMed: 23378830]

21. Budde MD, Frank JA. Examining brain microstructure using structure tensor analysis of histological sections. NeuroImage. 2012; 63(1):1–10. doi: http://dx.doi.org/10.1016/j.neuroimage.2012.06.042. [PubMed: 22759994]

22. Kemao AAQ. Characterizing young's fringes' orientation and spacing by fourier transform and radon transform. Optics & Laser Technology. 2002; 34(7):527–532. DOI: 10.1016/S0030-3992(02)00061-0

23. Lefebvre A, Corpetti T, Moy LH. Estimation of the orientation of textured patterns via wavelet analysis. Pattern Recognition Letters. 2011; 32(2):190–196. doi: http://dx.doi.org/10.1016/j.patrec.2010.09.021. URL http://www.sciencedirect.com/science/article/pii/S0167865510003259.

24. Michelet F, Germain C, Baylou P, da Costa J. Local multiple orientation estimation: isotropic and recursive oriented network. Pattern Recognition, 2004 ICPR 2004 Proceedings of the 17th International Conference on. 2004; 1:712–715. Vol.1. DOI: 10.1109/ICPR.2004.1334281

25. Choe AS, Stepniewska I, Colvin DC, Ding Z, Anderson AW. Validation of diffusion tensor mri in the central nervous system using light microscopy: quantitative comparison of fiber properties. NMR in Biomedicine. 2012; 25(7):900–908. URL http://dx.doi.org/10.1002/nbm.1810. DOI: 10.1002/nbm.1810 [PubMed: 22246940]

26. Bartsch H, Maechler P, Annese J. Automated determination of axonal orientation in the deep white matter of the human brain. Brain connectivity. 2012; 2(5):284–90. URL http://www.pubmedcentral.nih.gov/articlerender.fcgi?artid=3621296&tool=pmcentrez&rendertype=abstract. DOI: 10.1089/brain.2012.0096 [PubMed: 23030312]

27. Ortiz J, Hageman N, Salin A, Salin M, Dong H, Stark M, Vinters H, Toga A, Wisco J. Histological validation of the diffusion tensor: feasibility in human brain tissue. American Association of Anatomists (AAA) Abstr. 2010 Poster.

28. Liu R, Hageman N, Yang G, Cheng N, Chan K, Liu E, Ortiz J, Honarpisheh H, Wong A, Stark M, Dong H, Toga A, Vinters H, Wisco J. Anatomical validation of diffusion tensor imaging (dti). American Association of Anatomists (AAA) Abstr. 2013 Poster.

29. Damiani, E., Jeong, J., editors. Ch Simple low level features for image analysis. Springer; 2009. Multimedia Techniques for Device and Ambient Intelligence; p. 23

30. Lpez, F., Valiente, J., Baldrich, R., Vanrell, M. Ch Fast Surface Grading Using Color Statistics in the CIE Lab Space. Vol. 3523. Springer Berlin Heidelberg; 2005. Pattern Recognition and Image Analysis; p. 666-673.

31. Bansal S, Aggarwal D. Color Image segmentation using CIElab color space using Ant Colony optimization. International Journal of Computer Applications. 2011; 1(7):415–420. URL http://www.ijcset.net/docs/Volumes/volume1issue7/ijcset2011010715.pdf.

32. Rathore VS, Kumar MS, Verma A. Colour based image segmentation using l * a * b * colour space based on genetic algorithm. International Journal of Emerging Technology and Advanced Engineering. 2012; 2(6):156–162.

33. Selwal A, Sharma A. Evolution of Contour using Deformable Model in RGB, HSV and LAB Color Spaces. International Journal of Emerging Trends & Technology in Computer Science (IJETTCS). 2013; 2(2):290–295.

34. Baldevbhai PJ, Anand RS. Color image segmentation for medical images using l * a * b * color space. IOSR Journal of Electronics and Communication Engineering (IOSRJECE). 2012; 1(2):24–45.

35. Ghotkar A, Kharate G. Hand segmentation techniques to hand gesture recognition for natural human computer interaction. International Journal of Human Computer Interaction (IJHCI). 2012; 3(1):15–25. URL http://www.cs.olemiss.edu/~jxue/teaching/csci547_S14/notes/w5/IJHCI-38.pdf.
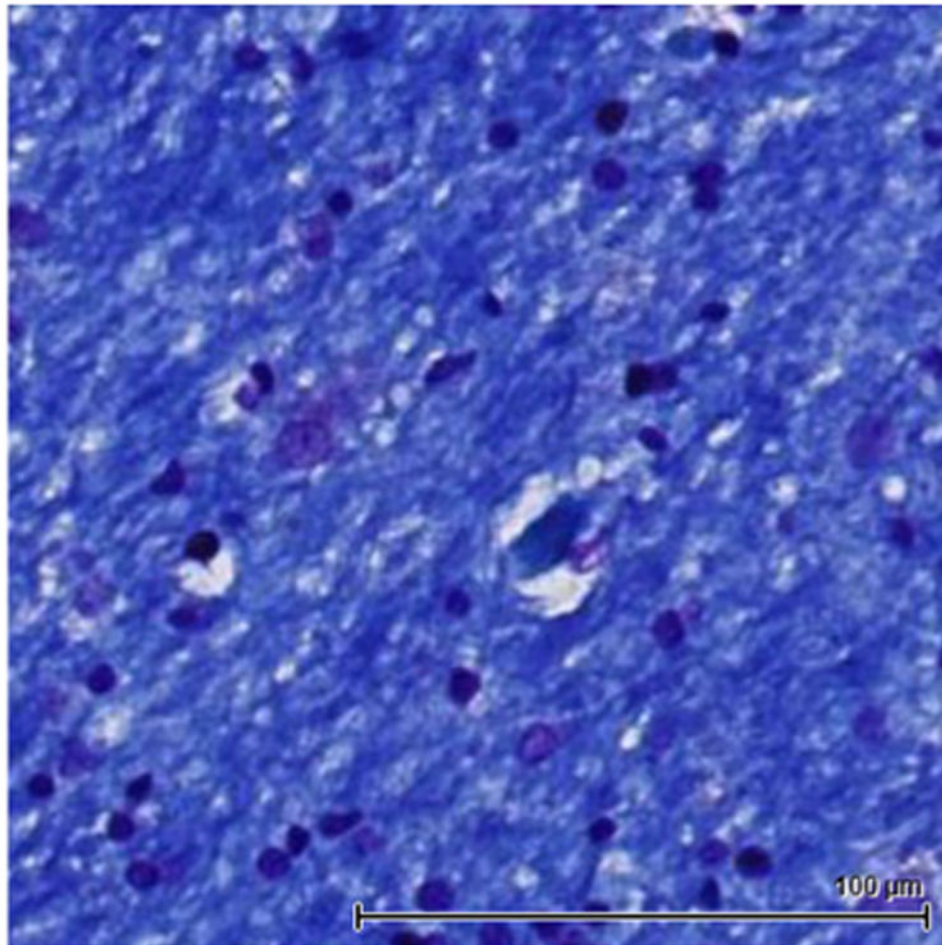
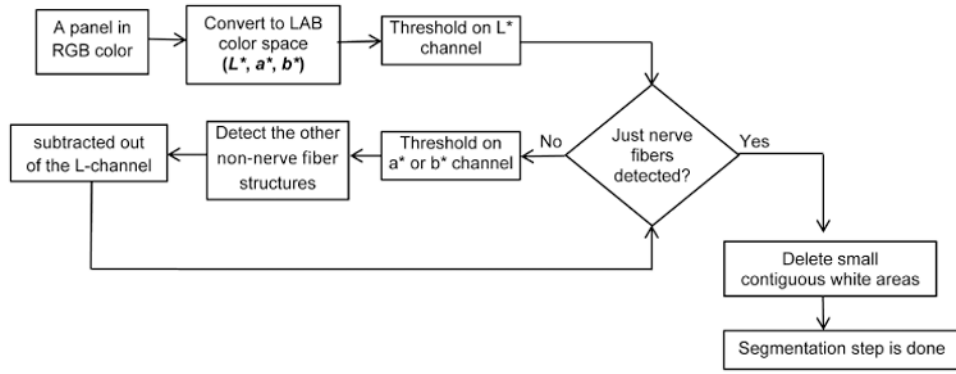**Figure 1. Histological sample of Luxol Fast Blue stained white matter in the medial temporal lobe**

Figure 2.
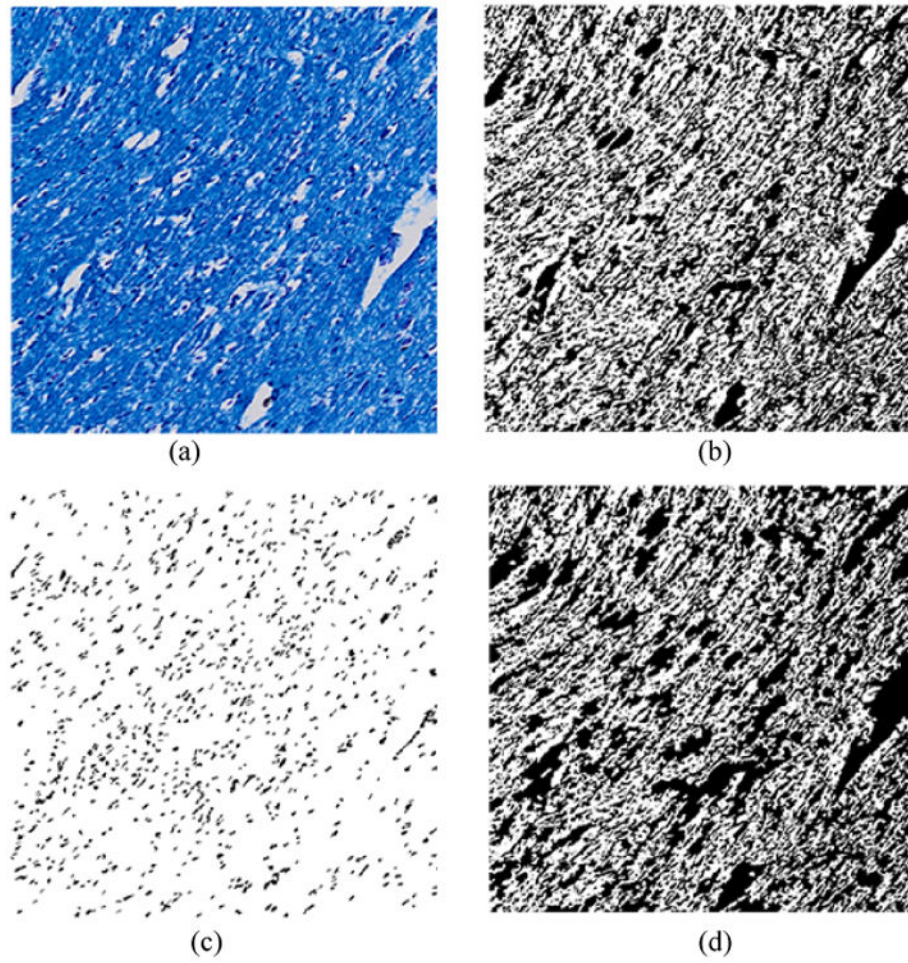Block diagram of the segmentation step.

Figure 3.
(a) A sample panel in the white matter of a histological slice. (b) Thresholding on L channel.
(c) Detected non-nerve fiber structures on a* channel. (d) Subtraction of (c) from (b). The remaining white structures in (d) are expected to correspond with nerve fibers.
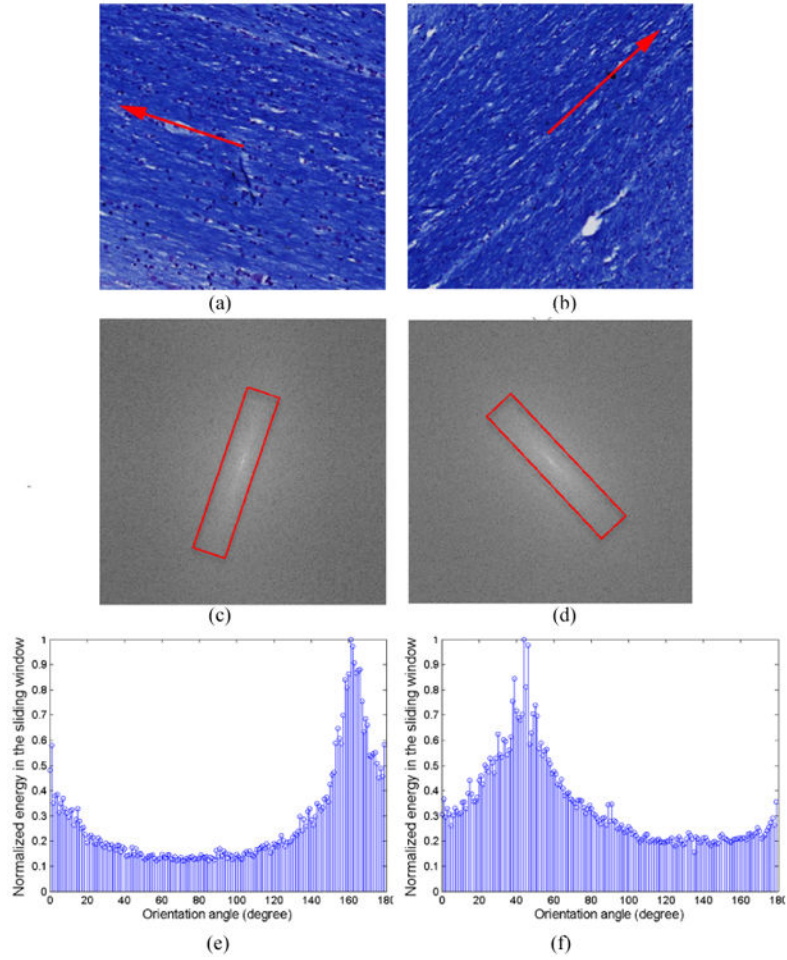
Figure 4.

(a) and (b) show two panels with different dominant nerve fiber directions; (c) and (d) show the magnitude of the 2D Fourier Transform of the segmented versions of figures (a) and (b), respectively. Regions of high energy have been illustrated by red rectangles. The fiber directions are perpendicular to the direction of the bright regions in the magnitude of the Fourier Transform. (e) and (f) represent angular orientation histograms extracted from (a) and (b), respectively. The peak in (e) and (f) represent the dominant nerve fiber orientation in (a) and (b), respectively.
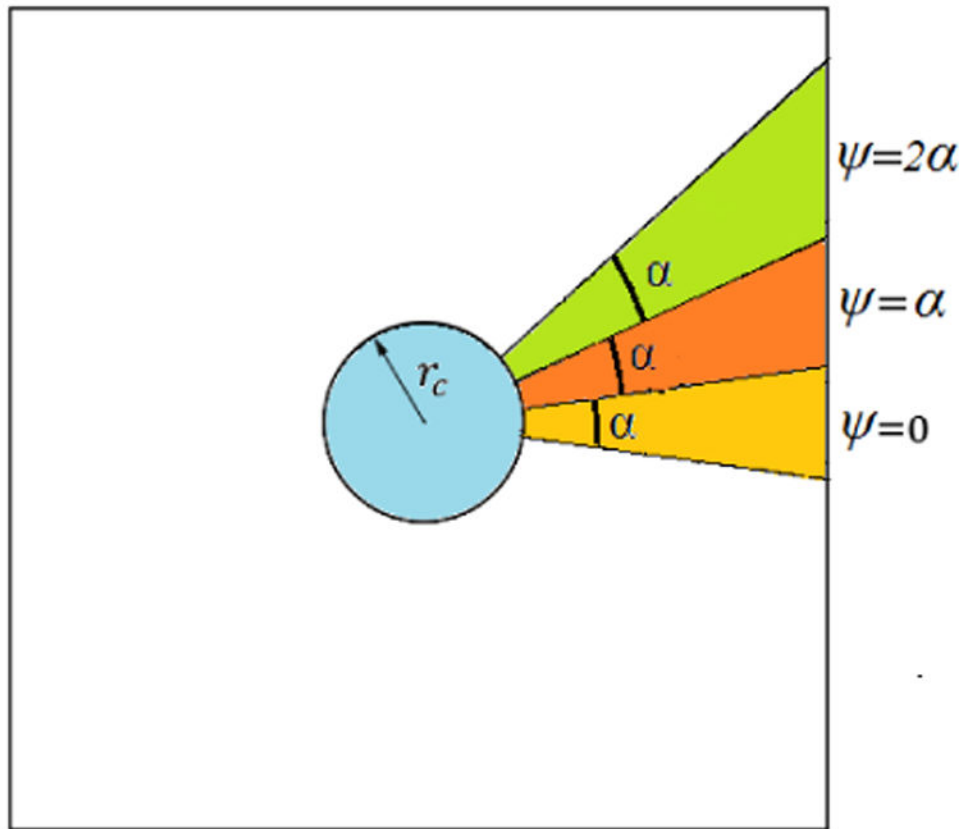
Figure 5.
Illustration of the calculation of image energy in angular window slices of the masked DFT panel image. The segmented panel is high pass filtered by zeroing out the center of the 2D DFT (the blue circle above). The energy in the 2D DFT image is then measured across different angular windows (3 shown). r_c is the cut off frequency, a is the angular window size, and Ψ is the angle of a radial line passing through the center of an angular window. In this figure, Ψ, the angular spacing between angular window slices is equal to the angular window size a.
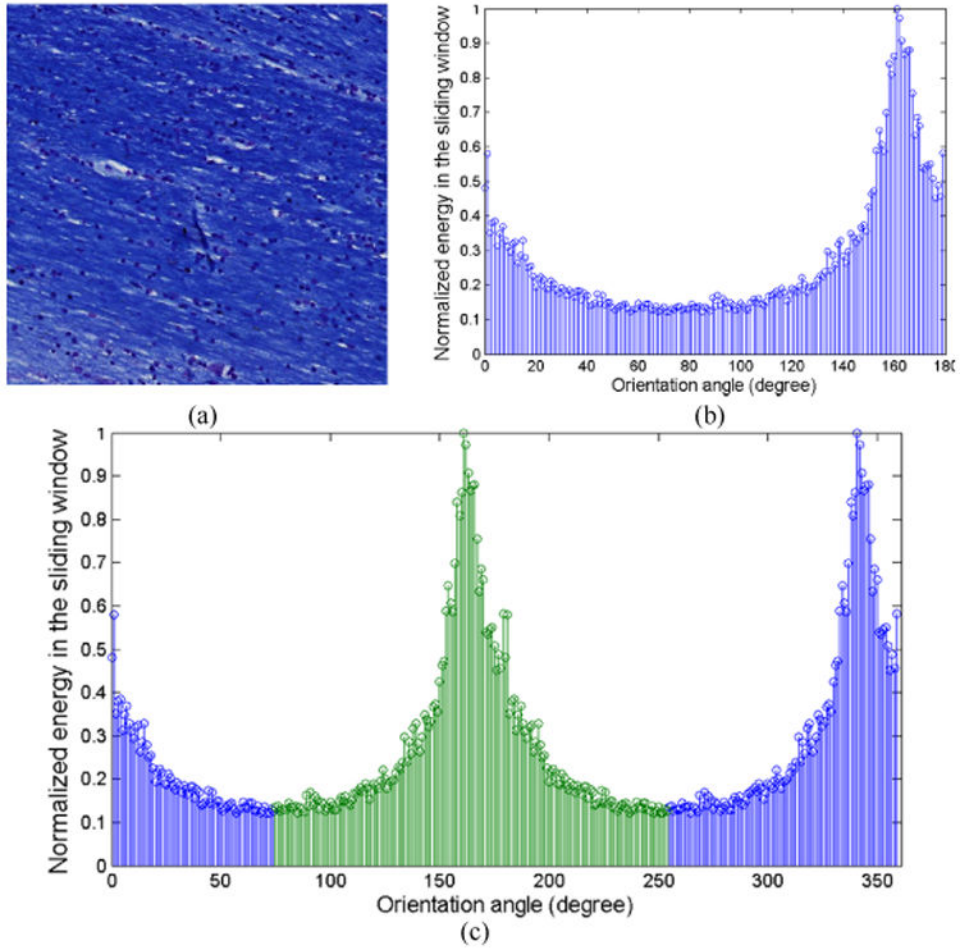
Figure 6.
(a) A sample panel in the white matter of a histological slice. (b) The histogram from 0 to 179 degrees yields a mean value of 104 degrees and standard deviation of 60 degrees, which is clearly not an accurate estimate. It is visually evident that the peak is centered closer to 165 degrees. Periodic extension of the angular histogram and identification of the sliding 180-degree window that yields the minimum variance across the window provides a much more robust way of identifying the center of the angular peak. This is illustrated in (c), where analysis of the mean on the 180-degree window shown in green (the minimum-variance window) yields a much more plausible mean value of 165 degrees.
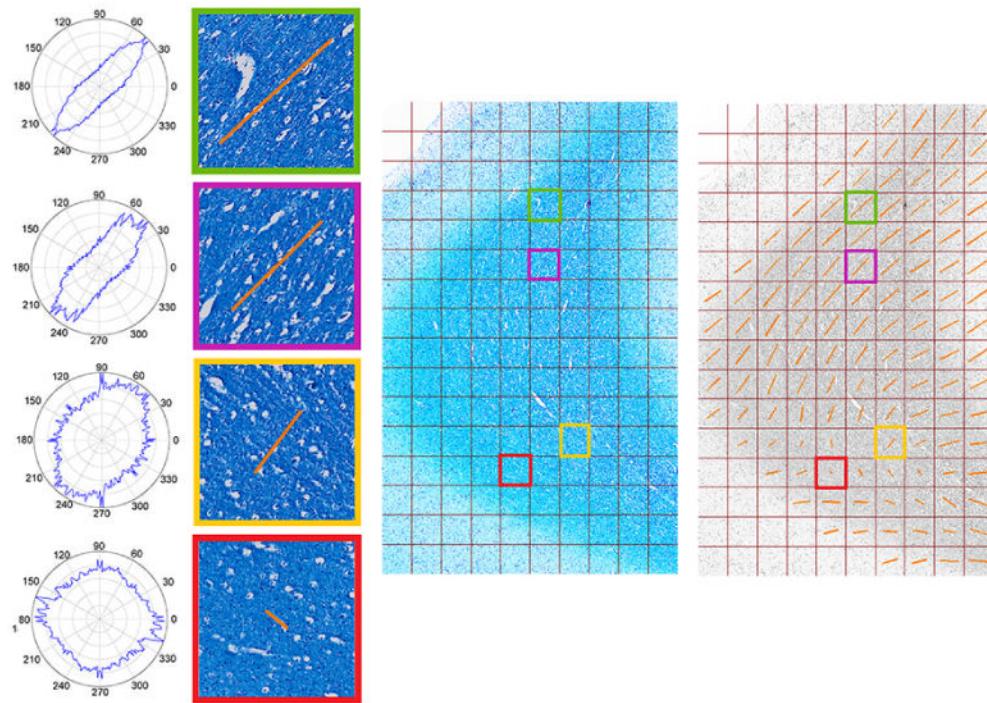
Figure 7.
A region of interest containing 123 panels, with the average orientation direction, calculated by the semi-automatic algorithm, shown as an arrow for each panel, constructed by the semi-automatic algorithm. The length of the line indicates the uncertainty in the angular estimate (lowerlength indicate a lower level of confidence in the angular estimate). It should be noted that DTI assigns a single directionality to the population of the nerve fibers, no matter if the fibers are parallel with each other, or not. Therefore, here, we keep defining the directionality of the nerve fibers with one direction although we have crossing fibers in some panels.

Table 1

Six histological slices (each from a different post-mortem brain) were used to validate the semi-automated algorithm. 300 panels were drawn from ROIs in the 6 histological slices, 50 from each histological slice, and were analyzed at variety of pixel sizes.

Data	Panel size (pixels)	Dimension of each panel (mm × mm)	Pixel size (mm × mm)	Number of panels	Maximum thresholding on *l* channel (Candela/pixel)	Minimum thresholding on *l* channel (Candela/pixel)
1	512 × 512	450 × 450	0.88 × 0.88	50	110;141	55;90
2	512 × 512	500 × 500	0.98 × 0.98	50	110;115;125	74;85
3	512 × 512	600 × 600	1.17 × 1.17	50	138;166	88;107
4	512 × 512	648 × 648	1.26 × 1.26	50	80;90	44;54
5	512 × 512	692 × 692	1.35 × 1.35	50	86;95;102	42;56;65
6	512 × 512	776 × 776	1.51 × 1.51	50	86;93	30;49